

## Supplementary material

### **Ferruginous phases in 19<sup>th</sup> century lime and cement mortars: a Raman microspectroscopic study.**

Petra Dariz<sup>a</sup> and Thomas Schmid<sup>b,c,\*</sup>

<sup>a</sup> Bern University of the Arts, Conservation-Restoration, Fellerstr. 11, 3027 Bern, Switzerland

<sup>b</sup> Federal Institute for Materials Research and Testing, Richard-Willstätter-Str. 11, 12489 Berlin, Germany; \* correspondence to [thomas.schmid@bam.de](mailto:thomas.schmid@bam.de)

<sup>c</sup> School of Analytical Sciences Adlershof (SALSA), Humboldt-Universität zu Berlin, Unter den Linden 6, 10099 Berlin, Germany

**Table S1: Measurement conditions of Raman maps and spectra.**

Figure	Laser wavelength	Laser power	Objective lens	Acquisition time (per pixel)
2c-d	532 nm	0.6 mW	100x/NA = 0.90	15 s
3, 2e (inset), S3	532 nm	0.6 mW	100x/NA = 0.90	120 s <sup>*)</sup>
4d, S4b-g, S4h-j	532 nm	0.6 mW	100x/NA = 0.90	10 s
5a, 5c-e, S5a-h	532 nm	3 mW	100x/NA = 0.90	10 s
6	632.8 nm	2 mW	50x/NA = 0.75	6 s
S2e, 2e	532 nm	0.6 mW	100x/NA = 0.90	10 s
S2f-g	532 nm	0.6 mW	100x/NA = 0.90	5 s
S4m-n	532 nm	1.5 mW	100x/NA = 0.90	6 s

<sup>\*)</sup> Single-spot spectra

**Table S2: Additional measurement parameters of Raman maps.**

Figure	Step size	Pixel number	Map size	Acquisition time (of whole map)
2c-d	400 nm	65 × 58 = 3770	26 μm × 23.2 μm	15.7 h
4d, S4b-g, S4h-j	1 μm	70 × 56 = 3920	70 μm × 56 μm	10.9 h
5a, 5c-e, S5a-h	1 μm	70 × 62 = 4340	70 μm × 62 μm	12.1 h
6	1 μm	83 × 91 = 7553	83 μm × 91 μm	12.6 h
S2e, 2e	1 μm	20 × 22 = 440	20 μm × 22 μm	1 h 13 min
S2f-g	400 nm	50 × 16 = 800	20 μm × 6.4 μm	1 h 7 min
S4m-n	1 μm	23 × 25 = 575	23 μm × 25 μm	58 min

**S1 Polarized light microscopy of ground iron slag admixed to lime mortar**

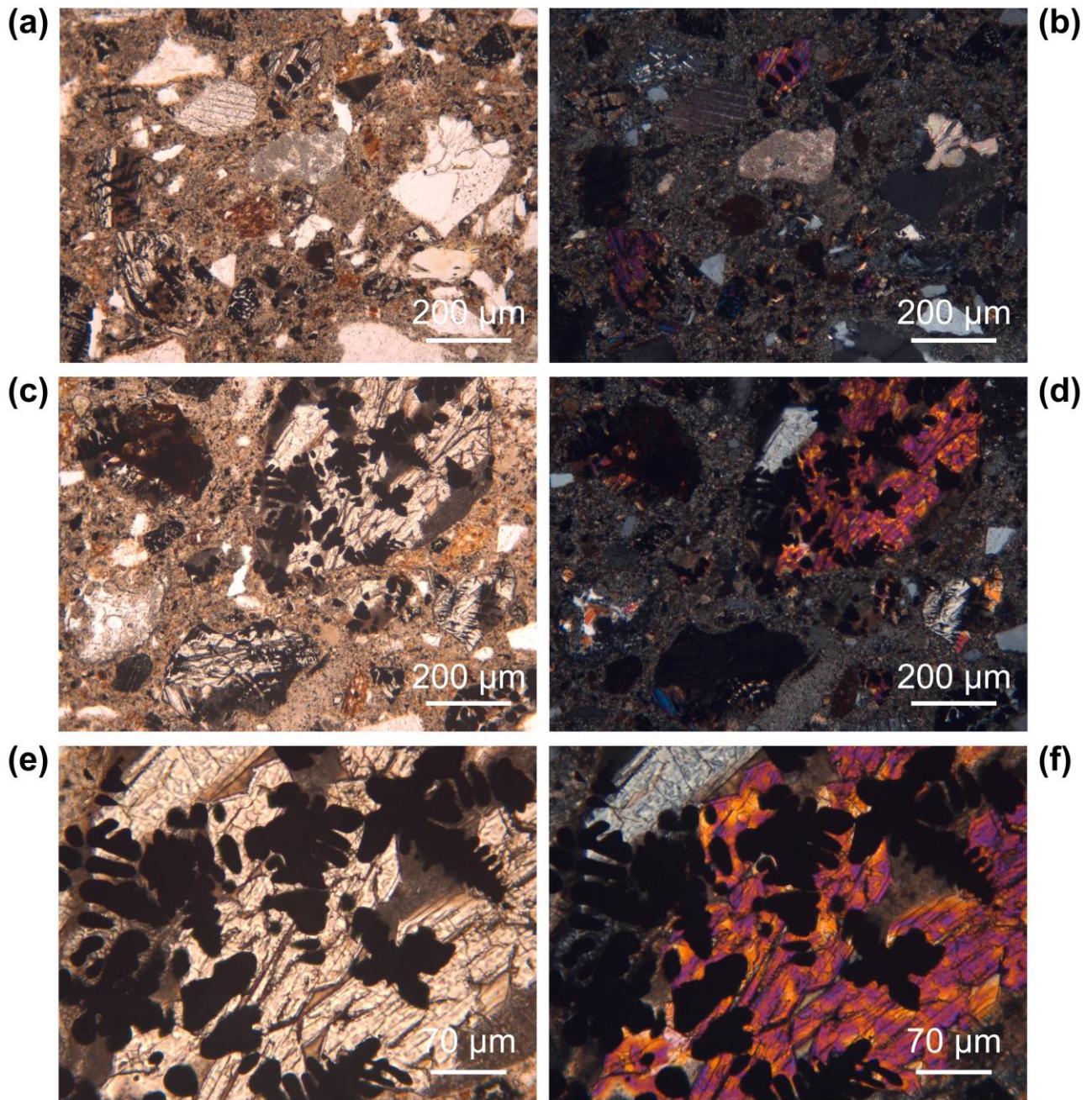


Fig. S1: Brightfield transmitted light microscopy images of pulverized slag (and powdered brick) used as mineral additives in a 19<sup>th</sup> century lime mortar under parallel (a, c, e) and crossed nicols (b, d, f).

## S2 Ferruginous phases in ground slag admixed to lime mortar: wuestite and olivine

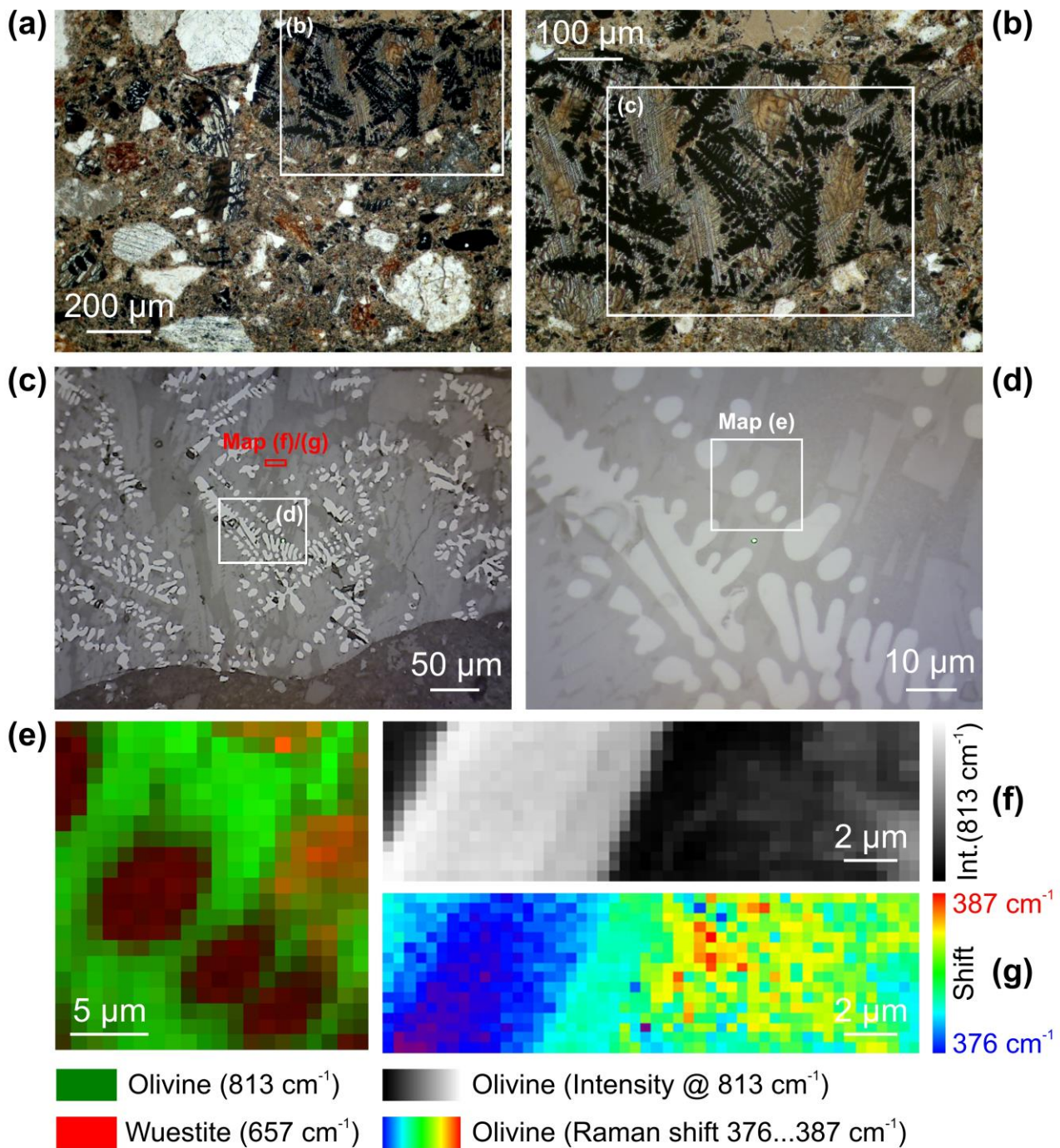


Fig. S2: Transmitted (a, b) and reflected light (c, d) microscopy images as well as Raman maps (e-g) of slag in lime mortar. (e) and (f) show Raman intensity distributions of olivine ( $813\text{ cm}^{-1}$ ) and wuestite ( $657\text{ cm}^{-1}$ ) marker bands, whereas (g) reveals the distribution of the Raman shift position of an olivine band, which allows to distinguish fayalite ( $376\text{ cm}^{-1}$ ) and kirschsteinite ( $387\text{ cm}^{-1}$ ).

As in Fig. 2, the Raman intensity map in Fig. S2e confirms that the dendritic structures (Fig. S2a-d) consist of wuestite overgrowing olivine. The Raman shift map (Fig. S2g) of a small excerpt, comprising parts of an olivine lath (left part of the image) and of the interstitial matrix, reveals zoning in the lath and intergrown crystals of different compositions in the ground mass. Wavenumbers between  $376\text{ cm}^{-1}$  (assigned to fayalite,  $\text{Fe}_2\text{SiO}_4$ ) and  $387\text{ cm}^{-1}$  (kirschsteinite,  $\text{CaFeSiO}_4$ ) might be due to intermediate sub-stoichiometric compositions (most likely in the lath) or due to superposition of bands of co-localized fayalite and kirschsteinite crystals.

### S3 Assignment of Raman spectra to fayalite, kirschsteinite and calciolivine

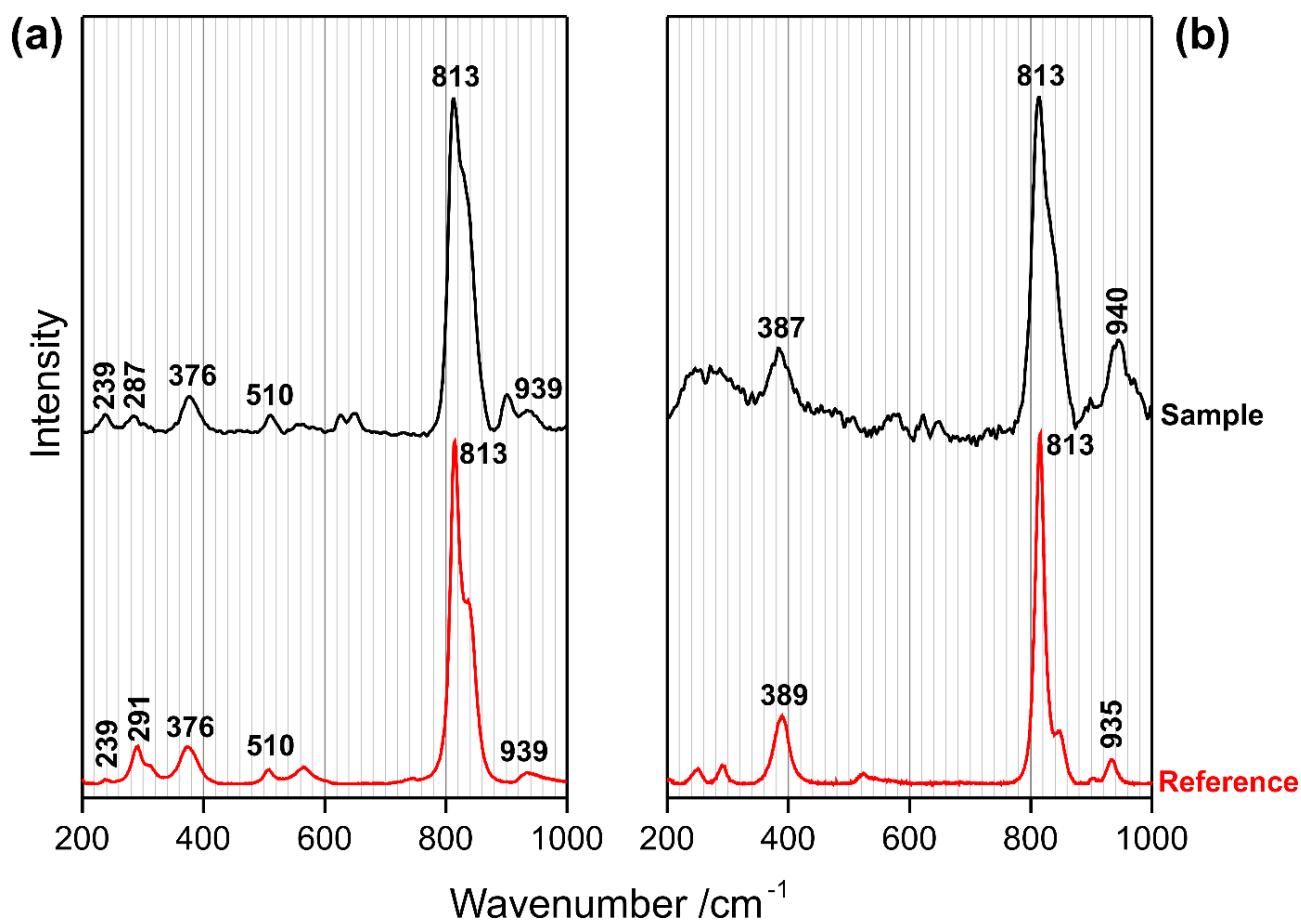


Fig. S3: Local single-spot Raman spectra of slag matrix in a lime mortar (black traces) and corresponding reference spectra of olivine (red traces). Sample spectrum (a) can be assigned to fayalite and sample spectrum (b) to kirschsteinite. The reference spectra of fayalite (a) and kirschsteinite (b) were taken from the RRUFF spectral database [S8].

As also shown in Fig. 3, the most prominent Raman band at 813 cm<sup>-1</sup> is (almost) the same for the three olivine group members fayalite (Fe<sub>2</sub>SiO<sub>4</sub>), kirschsteinite (CaFeSiO<sub>4</sub>) and calciolivine ( $\gamma$ -Ca<sub>2</sub>SiO<sub>4</sub>). By reviewing literature [S1-S7] and database spectra [S8], we found that a discrimination is possible based on the wavenumber position of a Raman band varying between 376 cm<sup>-1</sup> (fayalite), 387 cm<sup>-1</sup> (kirschsteinite) and  $\geq 400$  cm<sup>-1</sup> (calciolivine). This assignment is further evidenced by the accordance between further band positions in both, sample and reference database spectra [S8] as shown in Fig. S3. For example, in the fayalite spectrum, bands at 239 cm<sup>-1</sup>, approx. 290 cm<sup>-1</sup>, 510 cm<sup>-1</sup> and 939 cm<sup>-1</sup> are present in both, sample data and reference. Additional bands in the sample spectra are due to further phases present at the same sample spots. For example, the two (not labeled) bands at 626 cm<sup>-1</sup> and 658 cm<sup>-1</sup> can be assigned to melilite.

As there was no calciolivine spectrum available, neither in the RRUFF spectral database [S8] nor in our own collection of reference spectra gathered from synthesized clinker phases [S9], the assignment of calciolivine sample spectra in this study (as, for example, spectrum (1) in Fig. 3) was based on comparison of band positions with literature data [S1, S4-S5].

## S4 Ferruginous phases in residual Roman cement grains: hematite and esseneite

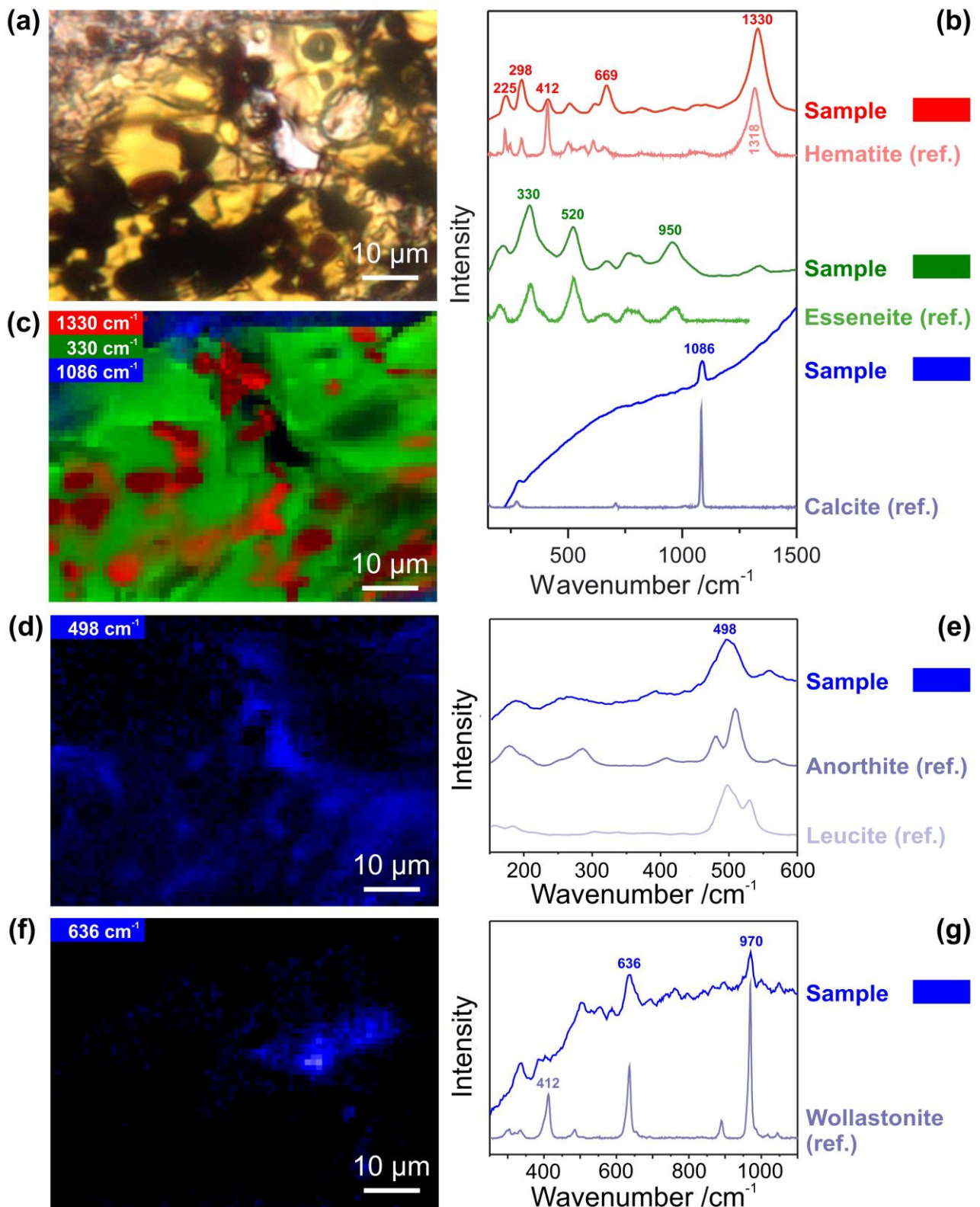


Fig. S4a-g: As an extension of Fig. 4 (main text), this figure shows the part of the transmitted light microscopy image (a) matching the area of the Raman map (c), the assignment of sample spectra to specific phases based on the comparison with reference database spectra [S8] (b), and the identification of the additional phases anorthite/leucite (d, e) and wollastonite (f, g).

Fig. S4a-g reveals the assignment of sample spectra to the phases hematite ( $\alpha$ -Fe<sub>2</sub>O<sub>3</sub>), esseneite (CaFeAlSiO<sub>6</sub>) and calcite (CaCO<sub>3</sub>) (see Fig. 4d in the main text) and adds the phase distributions of anorthite (CaAl<sub>2</sub>Si<sub>2</sub>O<sub>8</sub>)/leucite (KAlSi<sub>2</sub>O<sub>6</sub>) and wollastonite ( $\alpha$ -CaSiO<sub>3</sub>), identified by comparison with database spectra [S8] and/or literature data [S10]. The sample spectrum in Fig. S4e shows similarities to that of anorthite as well as leucite. An unambiguous discrimination of these two phases is not possible and the observed spectrum might even be interpreted as superposition of both reference spectra. Both anorthite and leucite are phases detected in residual overfired clinker phenograins in historical Roman cement mortars [S11].

Further to the visualization of microstructure and phase content of a preserved cement clinker particle, Fig. 4 in the main text allows a direct comparison of different microscopic techniques and their different intrinsic image contrasts. Whereas light microscopies rely on the local transmittance or reflectance of the sample with regard to visible light, the backscatter-electron imaging (BEI) contrast of an environmental scanning electron microscope (ESEM) mainly depends on local elemental composition, because electrons are backscattered more efficiently from sample areas consisting of elements of higher atomic number, which therefore appear brighter in BEI contrast. Thus, in this special case, the hematite droplets are clearly visible as bright spots because of their iron content, and the high BEI intensity (and optional elemental analysis by energy-dispersive X-ray spectroscopy (EDX)) together with the typical red hue in transmitted light microscopy additionally support the assignment of these microstructures to hematite.

Comparison of the different imaging techniques also reveals their different penetration depths. Only the top few 100 nm contribute to a BE image in electron microscopy, and the epi-illumination reflected light micrograph collected with the Raman microscope employed in this study appears quite similar, by coincidence also with the hematite aggregates appearing brightest. On the other hand, the sample over its almost whole thickness is visible in transmitted light microscopy. The penetration depth of Raman imaging lies somewhere between these extremes showing both, surface and sub-surface features, which becomes obvious when comparing the hematite droplets in the different image contrasts. Indeed, the depth resolution of the Raman microscope can optionally be changed by inserting a confocal pinhole into the beam path, but reduced signal intensity would have to be compensated with significantly longer mapping acquisition times in this case.

Combining electron microscopy with Raman microspectroscopy is an interesting analytical approach making use of complementary elemental (BEI, EDX) and phase analysis information (Raman). As demonstrated in Fig. 4, the same microstructures can be found even when performing ESEM and Raman measurements in a sequential manner with separate instruments, which opens up the possibility to add elemental EDX information to further studies. As Fig. 4 demonstrates, care has to be taken with the interpretation of complementary analytical data of such spatially heterogeneous samples. Even if combined instruments are used, and lateral spot sizes and spot locations can be perfectly matched, there will always be discrepancies between the penetration depths, because their local variations depend on independent sample properties (interaction with visible light vs. electron scattering). To our opinion, this might have played a hampering role in a study aiming to shed light on the varying local compositions of calcium aluminoferrites in a cross sectioned Portland cement clinker nodule by trying to correlate EDX data and Raman spectra collected with a combined instrument [S12].

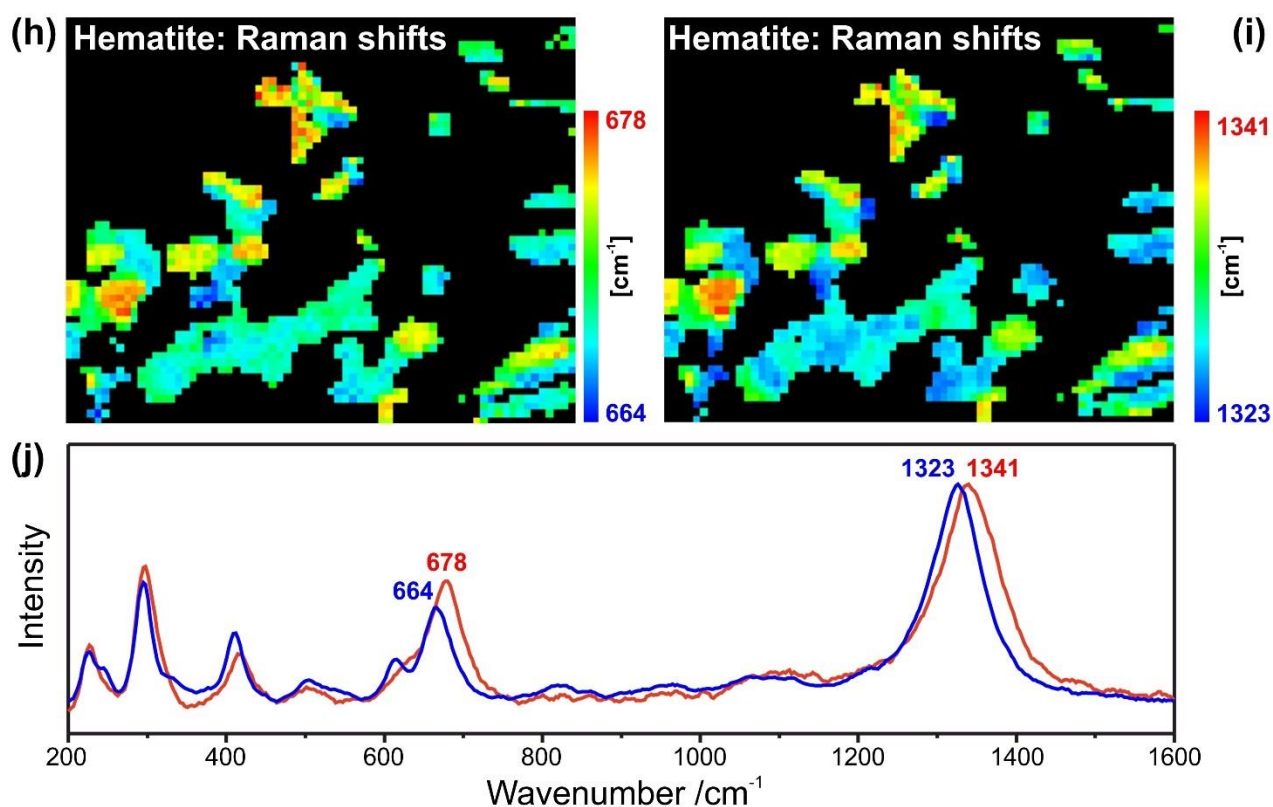


Fig. S4h-j: Local peak position shifts of hematite bands within the sample area shown in Figs. 4 and S4a-g. (j) shows that mainly the two bands of highest wavenumbers locally shift between 664  $\text{cm}^{-1}$ /1323  $\text{cm}^{-1}$  (lowest values, blue pixels in the maps) and 678  $\text{cm}^{-1}$ /1341  $\text{cm}^{-1}$  (highest values, red pixels). The local Raman shift positions of these two bands are shown in (h) and (i). In black pixels, no hematite spectrum was detected.

As already seen in Fig. S4b, the band positions in hematite spectra of the mortar sample under investigation in some cases differ from the reference database spectrum as most obviously seen for the most prominent second order band at 1318  $\text{cm}^{-1}$  in the reference and 1330  $\text{cm}^{-1}$  in the sample spectrum. Raman maps revealed that some hematite band positions change locally within the sample. As shown in Fig. S4h-j, this mainly concerns the two bands at 664-678  $\text{cm}^{-1}$  and at 1323-1341  $\text{cm}^{-1}$ , respectively. Obvious zoning patterns (and not just random pixel distributions) in the Raman maps confirm that this is not a measurement artifact, but reflects sample properties.

We explain these local Raman band shifts with the integration of foreign elements into the hematite crystal lattice. As described in the literature, implementation of  $\text{Al}^{3+}$  into  $\alpha\text{-Fe}_2\text{O}_3$  causes the appearance of a shoulder near 430  $\text{cm}^{-1}$  and of a band at approx. 670  $\text{cm}^{-1}$ ; the latter is sensitive to concentration-dependent shifts to higher wavenumbers [S13-S18]. This perfectly matches our observation, thus the generally higher Raman shifts of this (and the most prominent second order) band as compared to reference spectra could be explained with local concentration gradients of  $\text{Al}^{3+}$ , even though we cannot exclude that substitution of another foreign ion is responsible for the observed effect.

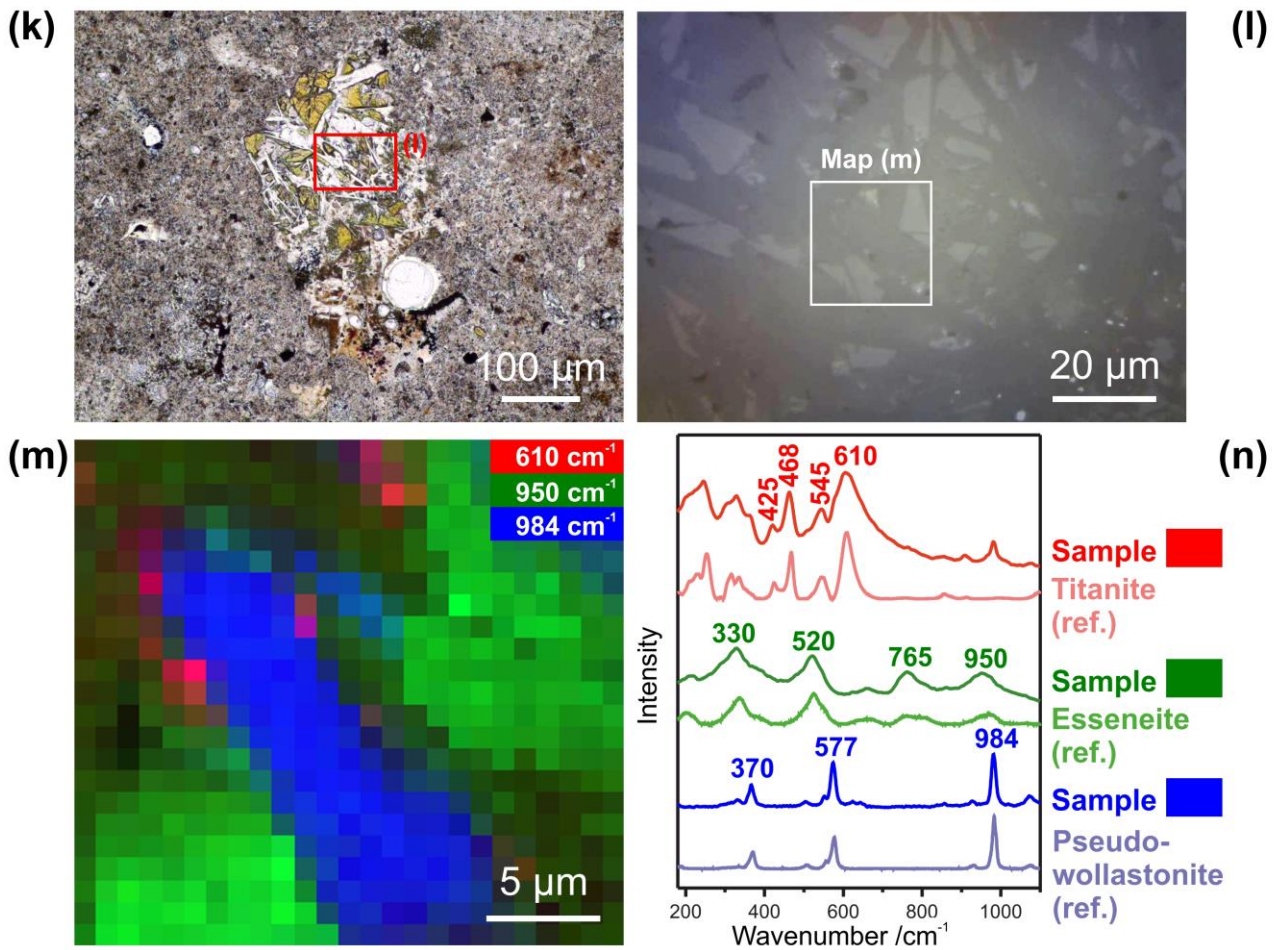


Fig. S4k-n: Raman map of another remnant clinker grain in Roman cement mortar. Transmitted (k) and reflected light (l) microscopy images, assignments of sample spectra to titanite, esseneite and pseudowollastonite via comparison with database spectra [S8] (n) and map of their distributions (m).

As shown in Fig. S4k-n, in another residual cement particle of the same Roman cement mortar sample the phases titanite ( $\text{CaTiSiO}_5$ ), esseneite ( $\text{CaFeAlSiO}_6$ ) and pseudowollastonite ( $\beta\text{-CaSiO}_3$ ) were identified by Raman microspectroscopic mapping.

**S5 Ferruginous phases in residual Roman cement particles: ferrosilite, srebrodolskite and brownmillerite**

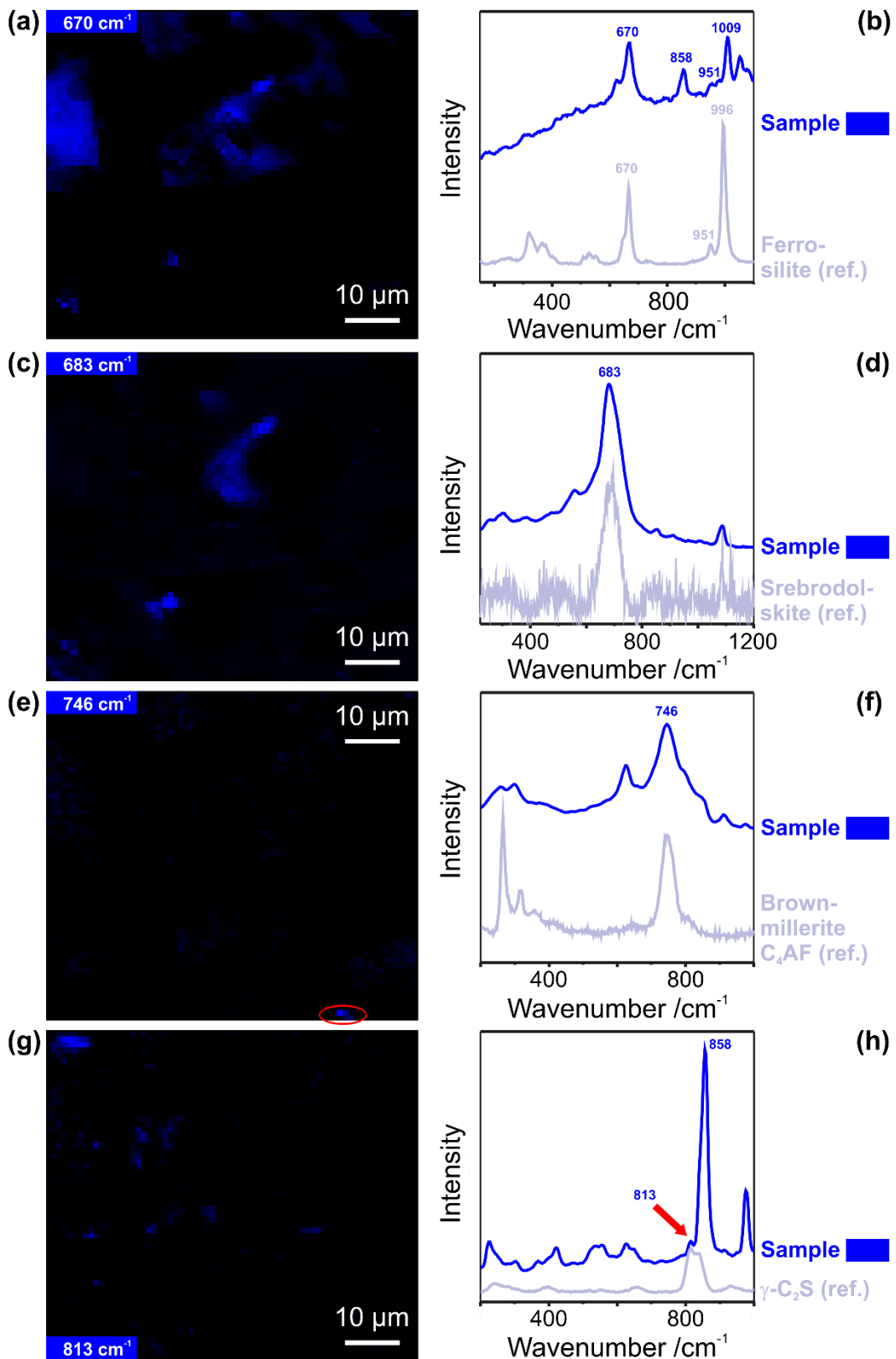


Fig. S5: As an extension of Fig. 5 (main text), this figure shows the identification of the additional phases ferrosilite ( $\text{FeSiO}_3$ ), srebrodolskite ( $\text{Ca}_2\text{Fe}_2\text{O}_5$  or in conventional cement notation  $\text{C}_2\text{F}$ ), brownmillerite ( $\text{Ca}_2\text{AlFeO}_5$  or  $\text{C}_4\text{AF}$ , respectively) and  $\gamma$ -belite ( $\gamma\text{-Ca}_2\text{SiO}_4$  or in conventional cement notation  $\gamma\text{-C}_2\text{S}$ ) in the Raman map displayed in Fig. 5.

## S6 Deviations of Raman spectra between natural minerals and corresponding synthetic phases

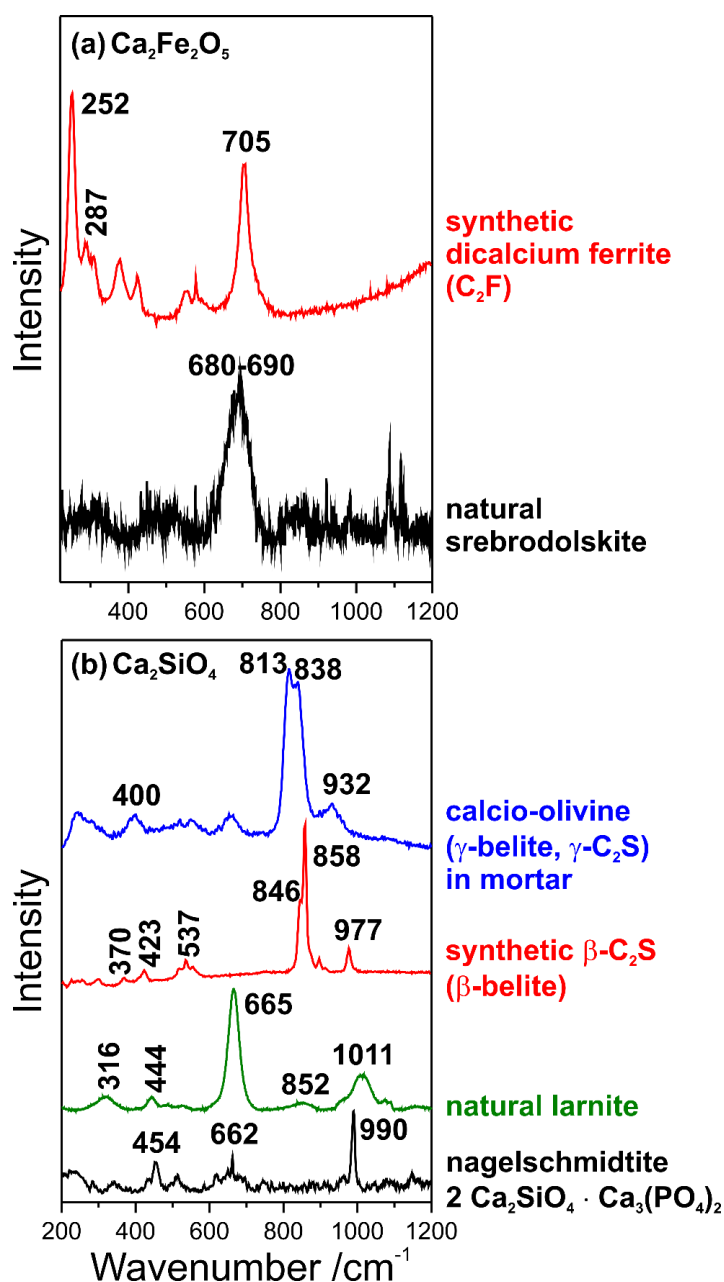


Fig. S6: Raman spectra of synthesized dicalcium ferrite (Ca<sub>2</sub>Fe<sub>2</sub>O<sub>5</sub>, in conventional cement notation C<sub>2</sub>F) and the mineral srebrodolskite as its natural counterpart (the latter was taken from the RRUFF spectral database [S8]) (a) and comparison of spectra of different dicalcium silicates of the sum formula Ca<sub>2</sub>SiO<sub>4</sub> (b).

Spectra resembling both, dicalcium ferrite (Ca<sub>2</sub>Fe<sub>2</sub>O<sub>5</sub> or C<sub>2</sub>F, respectively, Fig. 6b, d) and its natural counterpart, the mineral srebrodolskite (Fig. S5c, d) were found in residual Portland and Roman cement grains in 19<sup>th</sup> century mortars. The spectral differences shown in Fig. S6a are tentatively explained with the presence of foreign elements in the natural minerals, similar to natural larnite (Ca<sub>2</sub>SiO<sub>4</sub>) known often to be stabilized by phosphate and thus, spectroscopically better resembling the phosphate-containing nagelschmidite than synthetic β-Ca<sub>2</sub>SiO<sub>4</sub> (β-C<sub>2</sub>S or β-belite, respectively), which in turn is stabilized with Al<sub>2</sub>O<sub>3</sub> (Fig. S6b). Fig. S6 is discussed in more detail in the main text.

## References

- [S1] L. Black, Raman spectroscopy of cementitious materials, *Spectrosc. Prop. Inorg. Organomet. Compd.* 49 (2009) 72-127.
- [S2] S. Kramar, V. Tratnik, I. Hrovatin, A. Mladenović, H. Pristacz, N. Rogan Šmuc, Mineralogical and chemical characterization of Roman slag from the archaeological site of *Castra* (Ajdovščina, Slovenia), *Archaeometry* 57 (2015) 704-719.
- [S3] T. Mouri, M. Enami, Raman spectroscopic study of olivine-group minerals, *J. Miner. Petrol. Sci.* 103 (2008) 100-104.
- [S4] C. Remy, B. Reynard, M. Madon, Raman Spectroscopic Investigations of Dicalcium Silicate: Polymorphs and High-Temperature Phase Transformations, *J. Am. Ceram. Soc.* 80 (1997) 413-423.
- [S5] R. Stodolski, W. Pilz, Raman- und IR-spektroskopische Untersuchungen am Kilchoanit, *Z. Chem.* 23 (1983) 190-192.
- [S6] P. Schneider, P. Tropper, R. Kaindl, The formation of phosphoran olivine and stanfieldite from the pyromethamorphic breakdown of apatite in slags from a prehistoric ritual immolation site (Goldbichl, Igls, Tyro, Austria), *Miner. Petrol.* 107 (2013) 327-340.
- [S7] A. Chopelas, Single crystal Raman spectra of forsterite, fayalite, and monticellite, *Am. Mineral.* 76 (1991) 1101-1109.
- [S8] B. Lafuente, R. Downs, H. Yang, N. Stone, The power of databases: the RRUFF project, in: T. Armbruster, R. Danisi (Eds.), *Highlights in Mineralogical Crystallography*, W. de Gruyter, Berlin, 2015, pp. 1-29 (available on-line at <http://rruff.info/>).
- [S9] P. Dariz, J. Neubauer, F. Goetz-Neunhoeffler, T. Schmid, Clinker remnants in 19<sup>th</sup> century cement mortars indicating burning conditions – Comparing the Raman spectra of historic samples and modern synthesised calcium aluminates, *Eur. J. Mineral.* 28 (2016) 907-914.
- [S10] M. Conjeaud, H. Boyer, Some possibilities of Raman microprobe in cement chemistry, *Cem. Concr. Res.* 10 (1980) 61-70.
- [S11] J. Weber, N. Gademayer, D. Hughes, R. Kozlowski, M. Stillhammerova, D. Ullrich, R. Vyskocilova, Roman cement mortars in Europe's architectural heritage of the 19th century, *J. ASTM Int.* 4 (2007) 69-83.
- [S12] L. Black, A. Brooker, SEM-SCA: combined SEM-Raman spectrometer for analysis of OPC clinker, *Adv. Appl. Ceram.* 6 (2007) 327-334.
- [S13] A. Zoppi, C. Lofrumento, E. Castellucci, C. Dejoie, P. Sciau, Micro-Raman study of aluminium-bearing hematite from the slip of Gaul *sigillata* wares, *J. Raman Spectrosc.* 37 (2006) 1131-1138.
- [S14] A. Zoppi, C. Lofrumento, E. Castellucci, P. Sciau, Al-for-Fe substitution in hematite: the effect of low Al concentrations in the Raman spectrum of Fe<sub>2</sub>O<sub>3</sub>, *J. Raman Spectrosc.* 39 (2008) 40-46.
- [S15] D. Varnshey, A. Yogi, Structural and Electrical conductivity of Mn doped Hematite ( $\alpha$ -Fe<sub>2</sub>O<sub>3</sub>) phase, *J. Mol. Struct.* 995 (2011) 157-162.

- [S16] D. Varnshey, A. Yogi, Influence of Cr and Mn substitution on the structural and spectroscopic properties of doped haematite:  $\alpha\text{-Fe}_{2-x}\text{M}_x\text{O}_3$  ( $0.0 \leq x < 0.50$ ), *J. Mol. Struct.* 1052 (2013) 105-111.
- [S17] D. Varnshey, A. Yogi, Structural, vibrational and magnetic properties of Ti substituted bulk hematite:  $\alpha\text{-Fe}_{2-x}\text{Ti}_x\text{O}_3$ , *J. Adv. Ceram.* 3 (2014) 269-277.
- [S18] H. Liu, T. Chen, X. Zou, C. Qing, R. Frost, Effect of Al content on the structure of Al-substituted goethite: a micro-Raman spectroscopic study, *J. Raman Spectrosc.* 44 (2013) 1609-1614.